

CDW Gap Collapse and Weyl State Restoration in $(\text{TaSe}_4)_2\text{I}$ via Coherent Phonons: A First-Principles Study

Tao Jiang,^{1, 2, *} Jigang Wang,^{1, 3} and Yong-Xin Yao^{1, 3}

¹Ames National Laboratory, U.S. Department of Energy, Ames, Iowa 50011, USA

²Department of Materials Science and Nanoengineering, Rice University, Houston, Texas 77005, USA

³Department of Physics and Astronomy, Iowa State University, Ames, Iowa 50011, USA

Coherent phonon excitation offers a nonthermal route to control quantum phases of condensed matter. In this work, we employ first-principles calculations to investigate the phonon landscape of $(\text{TaSe}_4)_2\text{I}$ in its charge-density-wave (CDW) phase. We identify nine symmetry-preserving Raman-active modes that can suppress the Γ –Z direct gap to the meV scale and render the system globally gapless by generating Weyl nodes at generic k points. Among them, the 2.51 THz CDW amplitude mode $A(18)$ directly weakens the Ta-chain tetramerization, approaching a transient restoration of the uniform-chain geometry. It is also the most efficient mode owing to its low frequency and a relatively small critical displacement dominated by Ta motions. Other Raman modes, dominated by Se vibrations, require significantly larger displacements to reach the Weyl-semimetallic regime and are generally less effective than $A(18)$ at reducing the Ta-chain tetramerization. Furthermore, we explore nonlinear phonon–phonon interactions and find that the low-frequency infrared-active mode $B_3(7)$ (1.14 THz) exhibits strong anharmonic coupling with $A(18)$, providing an indirect pathway to drive the system toward a Weyl-semimetallic regime. Our results provide predictive insight for ultrafast pump–probe experiments and present a generalizable framework for lattice-driven topological switching in quasi-one-dimensional quantum materials.

I. INTRODUCTION

Charge density wave (CDW), characterized by a periodic modulation of the electronic density often coupled to the underlying lattice, can emerge in low-dimensional materials where reduced dimensionality enhances electron–phonon and electron–electron interactions [1–4]. In quasi-one-dimensional compounds like $(\text{TaSe}_4)_2\text{I}$, this collective ordering leads to a metal–insulator transition below 263 K, stabilized via Peierls-like lattice distortions [5–10]. The CDW phase exhibits rich emergent phenomena that manifest in nonlinear transport, tunable resistivity, and strong coherent lattice responses, which underpin diverse applications in electronic devices [11, 12], low-dissipation electron transport [13], photodetection [14, 15], THz emission [16], photo-elasticity [17] and phase change functionality [18], as well as emerging opportunities in nonlinear optics, such as high-order harmonic generation [19, 20].

These functional responses are grounded in a complex interplay among charge density waves, topological states [21–26], lattice chirality [27, 28], superconductivity [29, 30], structural disorder [31], and structural defects [32]. This multifaceted landscape has motivated various investigations into its temperature-dependent electronic structure, including experimental [33] and theoretical [34] studies. Although these works have provided valuable insights into the equilibrium properties of the CDW phase, important questions remain about the dynamic processes that govern its phase transitions.

Ultrafast spectroscopic techniques provide a powerful means to investigate the temporal evolution of CDW order, offering femtosecond-scale time resolution. Coherent

phonon excitation offers a nonthermal, symmetry-selective pathway to modulate quantum phases in solids [35, 36]. In particular, mode-selective phonon driving via both infrared [37, 38] and Raman channels [39, 40] has enabled ultrafast control of symmetry-breaking and topological transitions in a range of materials, including topological insulators [41–43], Dirac semimetals [44–46] and correlated CDW systems [47–49]. These advances underscore the importance of phonon-driven dynamics in future applications in high-speed electronics, spintronics, and quantum information technologies [50–52]. These insights motivate a focused investigation of coherent phonon dynamics in $(\text{TaSe}_4)_2\text{I}$.

Recent ultrafast experiments on this material have revealed a two-step response to optical excitation: rapid polaron melting, followed by modulation of the CDW order and chirality at picosecond timescales [53]. While the initial transition is driven by charge excitation and structural reorganization, the subsequent evolution involves mode-selective coherent phonons. However, these coherent phonons are not directly driven through mode-selective nonlinear coupling; rather, they appear to be a natural feedback response arising from the structural reorganization of the CDW state. This raises a compelling question: can symmetry-preserving coherent phonons themselves drive phase transitions in correlated complex materials?

In this work, we perform first-principles simulations to investigate the phonon landscape of $(\text{TaSe}_4)_2\text{I}$ in its CDW phase with a commensurate approximate structure. By evaluating the symmetry of each phonon mode and its effect on the electronic structure, we find that nine Raman-active modes, each of which preserves the entire crystal symmetry, can strongly suppress the minimum direct gap along the high-symmetry Γ –Z line to the meV scale, which

* tao.jiang@rice.edu

we use as a convenient indicator of CDW-gap quenching; meanwhile, Brillouin-zone-wide searches reveal the emergence of Weyl nodes at generic k points, establishing a globally gapless Weyl-semimetallic regime. Among them, we identify a 2.51 THz amplitude mode is the most efficient, requiring minimal atomic displacement and most effectively weakening the Ta-chain tetramerization toward a transient restoration of the uniform-chain geometry. By contrast, the Se-dominated Raman modes can also quench the electronic gap and induce a Weyl-semimetallic regime, but they do so with larger required displacements while leaving the underlying CDW lattice distortion largely intact. Furthermore, we explore nonlinear coupling between this Raman mode and low-frequency infrared-active phonons, identifying anharmonic pathways for indirect activation. Our results offer a microscopic mechanism for phonon-driven ultrafast control of CDW, and provide predictive guidance for time-resolved pump-probe experiments aiming to dynamically modulate quantum phases in the $(\text{TaSe}_4)_2\text{I}$ material.

II. METHOD AND MODEL SYSTEM

First-principles density functional theory (DFT) calculations were performed using the projector augmented-wave (PAW) method [54] and the Perdew–Burke–Ernzerhof (PBE) exchange-correlation functional [55], as implemented in the VASP package [56]. $(\text{TaSe}_4)_2\text{I}$ crystallizes in a tetragonal chiral structure with space group $I422$ (No. 97) under ambient conditions, with experimental lattice parameters $a = 9.531$ Å and $c = 12.824$ Å, corresponding to the non-CDW phase [57]. Structural optimization was carried out using a Γ -centered $3 \times 3 \times 2$ k -point mesh and a plane-wave cutoff energy of 400 eV, relaxing both lattice constants and atomic positions. The convergence criteria were set to 10^{-8} eV for electronic self-consistency and 0.01 eV/Å for ionic relaxation. The optimized lattice parameters for the tetragonal phase are $a = 9.769$ Å and $c = 12.950$ Å. We approximate the incommensurate CDW phase using an orthorhombic structure in space group $F222$ (No. 22), with optimized lattice parameters $a \approx b \approx 9.779$ Å and $c = 12.953$ Å, indicating a nearly tetragonal metric. A conventional cell containing 44 atoms (four formula units) was used to compute Γ -point phonons using the finite-displacement method implemented in PHONOPY [58]. Frozen-phonon band-structure calculations were performed in the primitive cell by displacing atoms along selected Γ -point phonon eigenvectors and computing the corresponding band structure using a Γ -centered $6 \times 6 \times 6$ k -point mesh. The crystal symmetry analysis was carried out using the spglib library [59] through its interface in pymatgen [60]. Optical activity analysis was carried out using the Bilbao Crystallographic Server [61]. Spin-orbit coupling was included in all calculations. Weyl points were computed by constructing a tight-binding model using maximally localized Wannier

TABLE I. Zone-center phonon modes of $(\text{TaSe}_4)_2\text{I}$ in the CDW phase, including vibrational frequencies (Freq), irreducible representations (Irrep), and optical activity. Also listed are the critical normal mode amplitudes (Q_c) with which the band gap along the Γ -Z path is reduced to its minimum value (a residual gap in the meV range), as well as the corresponding atomic displacements (D_c). Except for the $A(18)$ mode, where the largest displacement occurs on Ta atoms, the other modes exhibit dominant Se atom motion. These Raman-active phonon modes do not break the crystal symmetry and preserve the $F222$ space group. Additional phonon mode information is provided in Appendix Table A1.

Idx	Freq (THz)	Irrep	Activity	Q_c (Å $\sqrt{\text{amu}}$)	D_c (Å)	$E_G^{\min}(\Gamma\text{-Z})$ (meV)
18	2.51	A	Raman	2.5	0.098	3.0
30	4.07	A	Raman	6.3	0.270	1.1
33	4.23	A	Raman	3.5	0.149	2.2
40	4.82	A	Raman	6.7	0.293	2.0
41	4.84	A	Raman	4.1	0.170	2.0
44	5.08	A	Raman	3.8	0.162	4.0
47	5.34	A	Raman	4.8	0.179	2.4
50	5.50	A	Raman	3.3	0.134	0.5
62	7.84	A	Raman	6.6	0.264	3.3

functions [62, 63], and analyzing surface states using the surface Green’s function method implemented in the WannierTools package [64, 65].

III. CDW AMPLITUDE MODE

In the low-temperature CDW phase of $(\text{TaSe}_4)_2\text{I}$, the primitive cell contains 22 atoms (two formula units) and so it has 66 zone-center phonon modes with the following irreducible representations in the D_2 point group: $14A \oplus 18B_1 \oplus 16B_2 \oplus 18B_3$. Based on phonon symmetry analysis [61], phonon modes with the symmetries of B_1 , B_2 , and B_3 are both IR-active and Raman-active modes. Those modes with symmetry A are only Raman-active. Based on our frozen-phonon calculations, we observed that 9 of 14 zone-center A phonon modes could induce the transient phase transition from the gapped CDW phase to the Weyl semimetal. We refer to them as $A(18)$, $A(30)$, $A(33)$, $A(40)$, $A(41)$, $A(44)$, $A(47)$, $A(50)$ and $A(62)$, based on the energy ranking in the total 66 phonon modes with specific values shown in Table I. Note that Raman-active A modes are symmetry-preserving as the associated phonon displacements do not alter the crystal symmetry of space group $F222$. In contrast, distortions induced by modes with B_1 , B_2 , and B_3 break the symmetry, lowering the space group from $F222$ to $C2$. These symmetry relationships are summarized in Table A1.

Among these modes, the 2.51 THz Raman mode $A(18)$, which is the CDW amplitude mode, has the lowest frequency. This mode mainly involves Ta-atoms vibration along the chain direction as shown in Fig. 1 (a) and (b). The associated Ta atoms movement is the same as

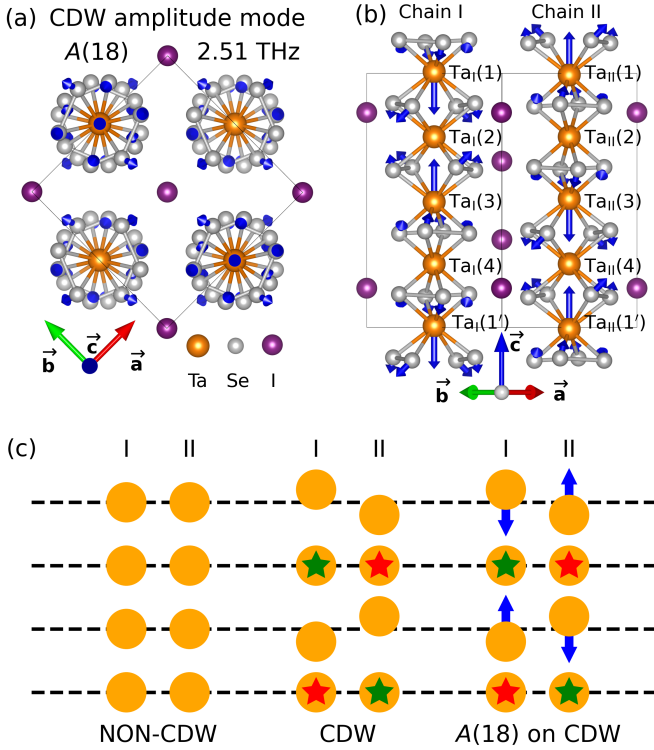


FIG. 1. (a) Top view and (b) side view of the conventional cell of $(\text{TaSe}_4)_2\text{I}$ in the CDW phase. Blue arrows indicate the eigenvectors of the 2.51 THz Raman-active mode $A(18)$, which preserves the $F222$ symmetry. (c) Schematic of Ta-chain tetramerization in three configurations: the non-CDW state (left), the CDW state (middle), and the CDW state distorted along the $A(18)$ eigenvector (right). Green stars mark the centers of the *long* Ta-Ta separations on the two chains: $\text{Ta}_1(1)$ – $\text{Ta}_1(3)$ on chain I (labeled at $\text{Ta}_1(2)$) and $\text{Ta}_{\text{II}}(3)$ – $\text{Ta}_{\text{II}}(1')$ on chain II (labeled at $\text{Ta}_{\text{II}}(4)$). Red stars mark the centers of the *short* Ta-Ta separations: $\text{Ta}_{\text{II}}(1)$ – $\text{Ta}_{\text{II}}(3)$ on chain II (labeled at $\text{Ta}_{\text{II}}(2)$) and $\text{Ta}_1(3)$ – $\text{Ta}_1(1')$ on chain I (labeled at $\text{Ta}_1(4)$). Here $\text{Ta}_1(1')$ and $\text{Ta}_{\text{II}}(1')$ denote the periodic images in the neighboring unit cell. Blue arrows illustrate the $A(18)$ -induced displacement pattern.

Ta-tetramerization of the CDW phase which breaks the symmetry of the isometric chain [66]. As illustrated in Fig. 1(c), the non-CDW phase exhibits equal distances between Ta atoms, while the CDW phase shows alternating long and short Ta-Ta distances. The green and red stars in Fig. 1(c) mark the centers of the long and short Ta-Ta separations on chains I and II, respectively. Our target amplitude mode $A(18)$ labeled as blue arrows at right sub-panel of Fig. 1 (c) modulates the Ta-Ta separations along the chains, reducing the long–short alternation and transiently driving the tetramerized pattern toward the nearly equal-spacing configuration of the non-CDW phase.

The $A(18)$ mode is experimentally observed at 2.6 THz [67, 68], consistent with our theoretical prediction. To investigate the electron-phonon coupling effect, we compute the dependence of electronic structure on

$A(18)$ phonon displacement with the frozen-phonon approximation. The evolution of the minimum direct gap along the high-symmetry Γ –Z as a function of the normal mode coordinate Q is shown in Fig. 2(a). Here, Q quantifies the atomic displacement along the $A(18)$ mode, with $Q = 1 \text{ \AA} \sqrt{\text{amu}}$ corresponding to a displacement of 0.039 \AA for the dominant $\text{Ta}_{\text{I,II}}(1,3)$ atoms. We use the minimum direct Γ –Z gap as a primary indicator because Γ –Z follows the quasi-one-dimensional chain direction in reciprocal space (along c^*) and captures the most pronounced CDW-induced gap opening in the low-temperature phase. Comparisons with other high-symmetry paths show that the Γ –Z gap is generally the most sensitive to the lattice distortion amplitude Q and is among the fastest to collapse (Appendix Fig. A1).

At equilibrium ($Q = 0$), the band structure exhibits a Γ –Z gap of 0.32 eV in Fig. 2(b). As the distortion amplitude increases, this Γ –Z gap gradually decreases and reaches its minimum value of 3.0 meV at $Q = 2.5 \text{ \AA} \sqrt{\text{amu}}$, as shown in Fig. 2(d), where the inset resolves the residual opening. Brillouin-zone-wide Weyl-node searches reveal 24 pairs of Weyl nodes at generic k points in this phonon-modulated structure shown in Fig. 2(f). Notably, Fig. 2(f) also shows that these nodes are not located exactly on the high-symmetry Γ –Z line. Upon lowering the symmetry from $I422$ to $F222$, the $C = \pm 2$ double Weyl nodes on Γ –Z are no longer symmetry-protected and are absent in our CDW structure [23, 69]. We find only $C = \pm 1$ Weyl nodes at generic k points, indicating that the double-Weyl degeneracy is lifted, potentially accompanied by node splitting and/or annihilation with opposite-chirality partners.

The strong gap suppression under $A(18)$ correlates with the modulated Ta-Ta separations. As shown in Table II, the $A(18)$ mode can transiently shorten the $\text{Ta}_1(1)$ – $\text{Ta}_1(3)$ separation from 6.635 \AA to 6.439 \AA at the gap-minimizing displacement, while lengthen the $\text{Ta}_{\text{II}}(1)$ – $\text{Ta}_{\text{II}}(3)$ separation from 6.318 \AA to 6.514 \AA . This brings the pairs of Ta-Ta atoms toward equal distance. However, at $Q = 2.5 \text{ \AA} \sqrt{\text{amu}}$, the Ta-Ta distances are not completely equivalent to those in the non-CDW phase. By monitoring the Ta-Ta separations as a function of Q , we find that the chain disproportionation is essentially removed at $Q = 2.0 \text{ \AA} \sqrt{\text{amu}}$, where the long and short Ta-Ta distances become nearly equal (i.e., a transient restoration of the uniform-chain geometry). At this distortion the Γ –Z gap is already suppressed to 5.8 meV [Fig. 2(c)], and a Brillouin-zone-wide Weyl-node search finds 12 pairs of Weyl nodes [Fig. 2(e)], indicating that the onset of semimetallic topology does not require the Γ –Z gap to be fully minimized. Upon increasing the amplitude further to $Q = 2.5 \text{ \AA} \sqrt{\text{amu}}$, the Γ –Z gap reaches its minimum and the number of Weyl-node pairs increases to 24 pairs [Fig. 2(f)].

To further clarify the microscopic origin, we analyzed element-resolved weights along Γ –Z and an element-selective decomposition of the $A(18)$ eigenvector (Appendix Figs. A2 and A3). The near-gap states are dom-

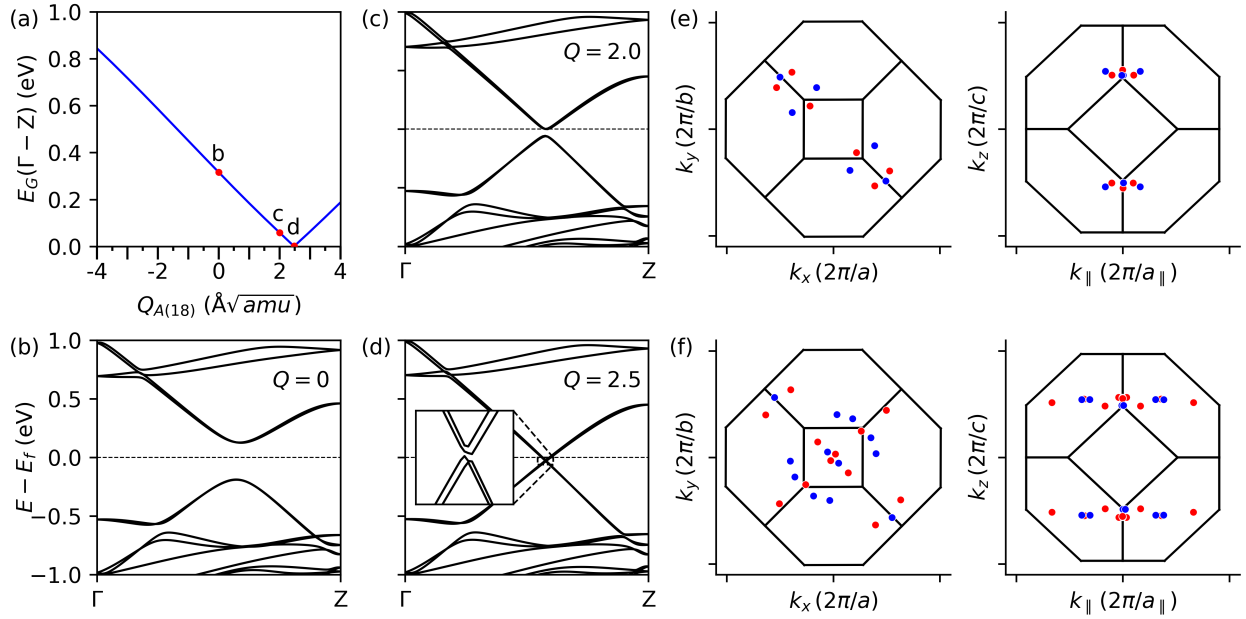


FIG. 2. (a) Phonon displacement-dependent band gap along Γ -Z in the CDW phase. Three red circles mark the $A(18)$ normal-mode amplitudes Q (in $\text{\AA}\sqrt{\text{amu}}$) corresponding to the band structures shown in panels (b) (c) and (d). (b) Electronic band structure along the high-symmetry path Γ -Z at equilibrium ($Q = 0$), showing a band gap of 0.32 eV. (c) Electronic band structure at $Q = 2.0$, where the Ta-Ta bond disproportionation (the long and short Ta-Ta distances become equal), indicating a transient restoration of the uniform-chain geometry (CDW melting in the structural sense); the Γ -Z gap is reduced to 5.8 meV. (d) Electronic band structure at $Q = 2.5$, where the minimum direct gap along Γ -Z is reduced to 3.0 meV. The inset magnifies the energy window $E - E_F \in [-0.06, 0]$ eV to resolve the residual gap. (e) Weyl nodes obtained from a Brillouin-zone-wide search for the phonon-modulated structure at $Q = 2.0$, projected onto the k_x - k_y plane (left) and the k_{\parallel} - k_z plane (right). (f) Same as (e) but for $Q = 2.5$. Red and blue spheres denote Weyl nodes with positive and negative chirality, respectively; all nodes shown lie within 10 meV of the Fermi level. Here $k_{\parallel} = (k_x + k_y)/\sqrt{2}$ is the in-plane momentum along the [110] direction, plotted in units of $2\pi/a_{\parallel}$ with $a_{\parallel} = \sqrt{a^2 + b^2}$.

TABLE II. Interatomic Ta-Ta separations (in \AA) in chain I and chain II for the non-CDW, CDW, and $A(18)$ -modulated structures. The $A(18)$ -modulated structure corresponds to the frozen-phonon distortion of the 2.51 THz Raman-active mode at $Q = 2.5 \text{\AA}\sqrt{\text{amu}}$, where the minimum direct Γ -Z gap is reduced to the meV scale.

Ta-Ta separation (\AA)	Non-CDW	CDW	$A(18)$ ($Q = 2.5$)
Ta _I (1) - Ta _I (3)	6.475	6.635	6.439
Ta _{II} (1) - Ta _{II} (3)	6.475	6.318	6.514
Ta _I (2) - Ta _I (4)	6.475	6.476	6.476
Ta _{II} (2) - Ta _{II} (4)	6.475	6.476	6.476

inated by Ta with a secondary Se contribution, while I is negligible. Consistent with this picture, the gap evolution under $A(18)$ is controlled mainly by Ta: when the distortion is restricted to Ta atoms (with the same normalization of Q), the minimum direct Γ -Z gap reaches the meV scale already at $Q = 2.0 \text{\AA}\sqrt{\text{amu}}$, compared with $Q = 2.5 \text{\AA}\sqrt{\text{amu}}$ for the full mode. By contrast, a Se-only distortion weakly *increases* the Γ -Z gap for $Q > 0$, partially compensating the Ta-driven gap reduction. Accordingly, the critical amplitude for the full $A(18)$ mode reflects a balance between Ta- and Se-selective con-

tributions rather than Ta-Ta geometry alone.

IV. SE-DOMINATED RAMAN MODES

In addition to the CDW amplitude mode $A(18)$, there are eight other Raman-active phonon modes that can strongly suppress the minimum direct gap along the high-symmetry Γ -Z line and drive the system into a globally gapless Weyl-semimetallic regime. In Fig. 3, for each mode, the first and second panels show the eigenvectors from the top and side views, respectively, and the third panel shows the evolution of the minimum direct Γ -Z gap as a function of the normal-mode coordinate Q . The corresponding electronic structures at the gap-minimizing (near-gap-closure) displacements are shown in the fourth panel. Each mode exhibits a distinct critical displacement Q_c required to reach the near-closure condition, as summarized in Table I. Along the high-symmetry Γ -Z line, the near-gap bands approach each other closely, leaving only a meV-scale residual gap, indicating that the near-closure occurs in the vicinity of this line. Meanwhile, Brillouin-zone-wide node searches identify Weyl nodes at generic k points (fifth panel) rather than exactly on Γ -Z. This is

expected because the phonon-induced distortion lowers the crystal symmetry, removing the symmetry constraints that would otherwise pin band-touching points (Weyl nodes) to high-symmetry lines. In particular, mode A(50) shows an especially strong near-closure along Γ –Z (sub-meV residual gap), and the resulting Weyl nodes are found very close to this line, although they remain slightly off Γ –Z when their coordinates are examined.

Notably, unlike the CDW amplitude mode $A(18)$, these Se-dominated distortions do not necessarily imply a pronounced reduction of the Ta-chain tetramerization, suggesting that electronic gap quenching can occur even when the underlying CDW lattice distortion largely persists. A common characteristic across all modes is that the largest atomic displacements primarily originate from Se vibrations. However, the required maximum atomic displacements D_c are substantially larger than that of the CDW amplitude mode, and these modes occur at higher frequencies up to 5.5 THz. In fact, Table I shows that several Se-dominated modes (e.g., $A(30)$, $A(40)$, and $A(62)$) require $D_c \gtrsim 0.2$ Å, i.e., lattice-scale displacements that are likely difficult to achieve coherently without substantial heating or structural damage. Therefore, in the next section discussing IR-coupled Raman processes, we primarily focus on the CDW amplitude mode, as it presents a more experimentally feasible path for driving the insulator-to-semimetal transition [70].

V. NONLINEAR PHONON COUPLING BETWEEN CDW AMPLITUDE MODE AND IR MODES

Nonlinear phononic coupling has emerged as a powerful mechanism for manipulating lattice dynamics and electronic phases in quantum materials [71]. Recent studies have shown that intense THz excitation can trigger coherent energy transfer across vibrational modes due to mode-selective coupling, enabling ultrafast control of structural and electronic properties [72–75]. A particularly important class of such interactions involves the excitation of an IR-active phonon that drives a unidirectional displacement in a Raman-active mode via anharmonic coupling. This IR–Raman mechanism forms the basis for dynamical control of structural and electronic phase transitions, including magnetic and topological states, as demonstrated in recent theoretical studies [76–78].

In this section, we investigate the nonlinear phononic mechanism in $(\text{TaSe}_4)_2\text{I}$ by identifying IR-active modes that couple anharmonically to the Raman-active CDW amplitude mode $A(18)$. This low-frequency Raman mode is primarily responsible for strongly suppressing the CDW gap and restoring Weyl semimetal features, making it a central target for coherent phonon control. To quantify the coupling, we performed total energy calculations as a function of an IR mode and $A(18)$ normal coordinates to construct two-dimensional energy surfaces. These potential energy surfaces were then fitted using

a fourth-order anharmonic expansion that explicitly captures mode–mode interactions and nonlinear effects [79–81]:

$$V(Q_{\text{IR}}, Q_{\text{R}}) = \frac{\omega_{\text{IR}}^2}{2} Q_{\text{IR}}^2 + \frac{\omega_{\text{R}}^2}{2} Q_{\text{R}}^2 + \frac{c_1}{3} Q_{\text{IR}}^3 + \frac{c_2}{3} Q_{\text{R}}^3 + c_{12} Q_{\text{IR}} Q_{\text{R}}^2 + c_{21} Q_{\text{IR}}^2 Q_{\text{R}} + \frac{d_1}{4} Q_{\text{IR}}^4 + \frac{d_2}{4} Q_{\text{R}}^4 + d_{13} Q_{\text{IR}} Q_{\text{R}}^3 + d_{31} Q_{\text{IR}}^3 Q_{\text{R}} + d_{22} Q_{\text{IR}}^2 Q_{\text{R}}^2 \quad (1)$$

where Q_{IR} is the amplitude of an IR mode, and Q_{R} is the amplitude of the Raman mode. The first two terms represent the harmonic potentials for the IR and Raman normal modes, with ω_{IR} and ω_{R} being their respective eigen-frequencies. The cubic terms (c_1 , c_2) describe intrinsic intra-mode anharmonicity, while c_{12} and c_{21} represent third-order IR–Raman coupling strengths. The quartic terms (d_1 , d_2) account for higher-order intra-mode coupling, and d_{13} , d_{31} , and d_{22} describe fourth-order anharmonic coupling between the modes. By symmetry, the lattice potential must be invariant under the operations of the reference structure. Because the IR mode considered here has B symmetry, its normal coordinate changes sign under the symmetry operation(s) that leave the A -symmetry Raman coordinate unchanged. Therefore, all terms containing an odd power of Q_{IR} are forbidden, i.e., $c_1 = c_{12} = d_{13} = d_{31} = 0$, consistent with our numerical fits. The potential thus simplifies to

$$V(Q_{\text{IR}}, Q_{\text{R}}) = \frac{\omega_{\text{IR}}^2}{2} Q_{\text{IR}}^2 + \frac{\omega_{\text{R}}^2}{2} Q_{\text{R}}^2 + \frac{c_2}{3} Q_{\text{R}}^3 + c_{21} Q_{\text{IR}}^2 Q_{\text{R}} + \frac{d_1}{4} Q_{\text{IR}}^4 + \frac{d_2}{4} Q_{\text{R}}^4 + d_{22} Q_{\text{IR}}^2 Q_{\text{R}}^2 \quad (2)$$

In particular, the $c_{21} Q_{\text{IR}}^2 Q_{\text{R}}$ and $d_{22} Q_{\text{IR}}^2 Q_{\text{R}}^2$ terms quantify the ability of an IR-active phonon to drive unidirectional displacements in the Raman mode, which is key for coherent control. The $c_{21} Q_{\text{IR}}^2 Q_{\text{R}}$ term enables rectification of the oscillatory IR mode into a directional force on the Raman mode, as discussed in theoretical proposals for light-induced structural transitions [79, 80]. Meanwhile, the $d_{22} Q_{\text{IR}}^2 Q_{\text{R}}^2$ term modulates the phonon energy landscape and can enhance or suppress the IR–Raman interaction depending on the mode symmetry and excitation strength, as demonstrated in studies of magnetophononic switching and light-induced phase control [81].

We computed the anharmonic coupling coefficients between all IR-active modes and the Raman-active CDW amplitude mode $A(18)$. The complete dataset is presented in Appendix Table A2, while the results of some most representative IR modes are summarized in Table III. For example, $B_2(8)$, $B_3(9)$ (both near 1.3 THz), and $B_3(17)$ [53] exhibit weak anharmonic coupling with $A(18)$, as evidenced by their small c_{21} and d_{22} coefficients. In contrast, $B_3(7)$, $B_3(34)$, $B_3(42)$, and $B_1(54)$ show significantly stronger anharmonic interactions, particularly

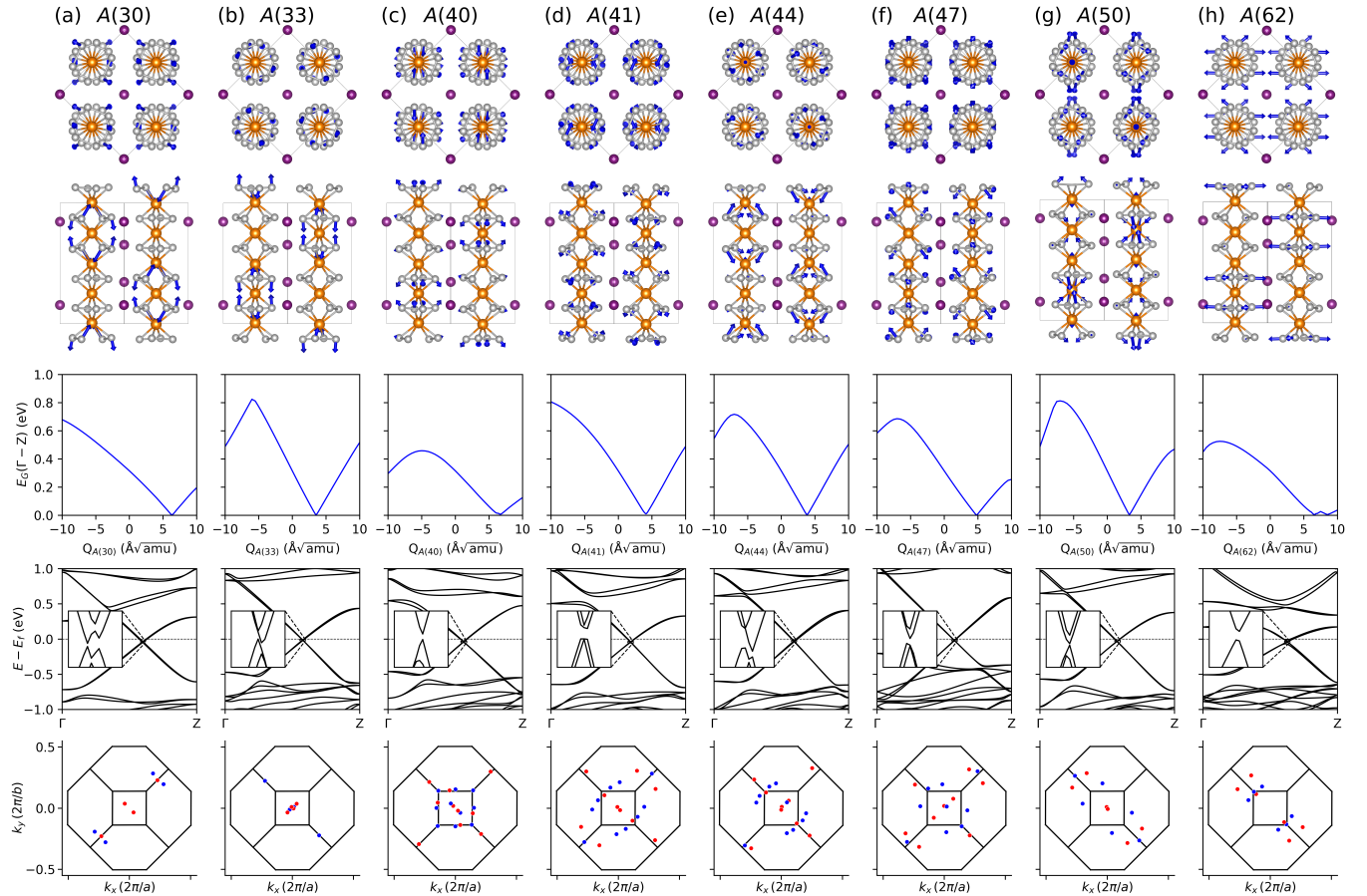


FIG. 3. Phonon-driven Γ –Z gap suppression in $(\text{TaSe}_4)_2\text{I}$ by Raman-active modes beyond the CDW amplitude mode. (a–h) Results for eight representative Raman-active modes: $A(30)$, $A(33)$, $A(40)$, $A(41)$, $A(44)$, $A(47)$, $A(50)$, and $A(62)$, respectively. For each mode, the *first* and *second* panels show the phonon eigenvectors in the top and side views, respectively; blue arrows indicate the atomic displacement directions, with dominant motion observed on Se atoms. The *third* panels show the evolution of the band gap along the Γ –Z path as a function of the normal mode coordinate Q , showing that each mode can suppress the gap to the meV scale at a mode-dependent near-closure amplitude Q_c (Table I). The *fourth* panels present corresponding electronic band structures along Γ –Z at $Q = Q_c$, showing a near-touching along Γ –Z with a meV-scale residual gap. Insets zoom into the near- E_F energy range to resolve the meV-scale residual opening; the energy window is chosen individually for each mode for clarity. The *fifth* panels show Brillouin-zone-wide Weyl-node searches for the phonon-distorted structures at $Q = Q_c$, showing that the Weyl nodes occur at generic k points rather than exactly on the Γ –Z line.

through the c_{21} and d_{22} terms. Among these, $B_3(7)$ stands out due to its especially large d_{22} coefficient. Moreover, its low vibrational frequency makes $B_3(7)$ energetically favorable for excitation, identifying it as a promising candidate for experimental control of the CDW amplitude mode through IR–Raman anharmonic coupling.

The eigenvectors of the $B_3(7)$ mode are shown in Fig. 4(a) and (b) from the top and side views, respectively. This mode primarily involves vibrations of Ta atoms along the c -axis, similar to the Raman $A(18)$ mode. A direct comparison between $B_3(7)$ and $A(18)$ is illustrated in Fig. 4(d). Note that $B_3(7)$ breaks the two-fold rotation symmetries about the x and y axes and lowers the space group from $F2\bar{2}2$ to $C2$, whereas the $A(18)$ distortion preserves these symmetries and leaves the space group unchanged ($F2\bar{2}2$) (see Appendix Table A1).

We can further demonstrate the strong anharmonic

coupling between the $A(18)$ Raman mode and $B_3(7)$ IR mode by plotting the potential energy curve of $A(18)$ dependent of finite $B_3(7)$ displacement, as presented in Fig. 4(c). The black dashed line with the normal mode coordinate $Q_{B_3(7)} = 0$ represents the baseline potential energy curve of $A(18)$ in the absence of IR distortion. The orange dashed line ($Q_{B_3(7)} = \pm 1.0$) shows a slight stiffening of the energy profile, while the blue dashed line ($Q_{B_3(7)} = \pm 2.0$) reveals a noticeably steeper curvature.

These results show that excitation of the $B_3(7)$ IR-active mode significantly alters the potential energy profile of the $A(18)$ Raman mode, confirming strong anharmonic coupling between them. As the $B_3(7)$ amplitude increases, the $A(18)$ potential energy curve is modified more substantially, consistent with substantial contributions from fourth-order coupling terms with sizable d_{22} , in the phonon–phonon interaction energy. This establishes

TABLE III. Anharmonic coupling coefficients between selected IR-active phonon modes and the Raman-active CDW amplitude mode $A(18)$ in $(\text{TaSe}_4)_2\text{I}$. Listed are the mode indices, frequencies (THz), irreducible representations, and symmetry-allowed third- and fourth-order coefficients (c_2 , c_{21} , d_1 , d_2 , d_{22}) extracted from the nonlinear energy expansion in Eq. (2). Energies used in the fitting are in meV per atom; coefficients are in $\text{meV}/(\text{amu}^{k/2}\text{\AA}^k)$, where k is the total order of displacements ($k = 3$ for cubic and $k = 4$ for quartic terms).

Idx	Freq	Irrep	c_2	c_{21}	d_1	d_2	d_{22}
7	1.14	B_3	0.188	0.080	-0.022	0.002	0.011
8	1.27	B_2	0.199	-0.004	0.065	0.003	-0.001
9	1.29	B_1	0.199	-0.002	0.066	0.003	-0.002
17	2.01	B_3	0.198	0.003	0.057	0.003	-0.001
34	4.30	B_3	0.198	-0.076	0.069	0.003	0.001
42	4.84	B_3	0.198	0.087	0.063	0.003	-0.004
54	5.87	B_1	0.198	0.070	0.064	0.003	-0.005

$B_3(7)$ as a promising candidate for indirect control of the CDW amplitude mode through selective IR excitation and Raman mode-coupling in pump–probe experiments.

In addition to the curvature enhancement, we observe a slight shift of the $A(18)$ potential minimum toward negative Q_R values as the $B_3(7)$ amplitude increases. This asymmetric displacement is consistent with the third-order coupling term $c_{21}Q_{\text{IR}}^2Q_R$ with $c_{21} > 0$, which rectifies the IR phonon oscillation into a net directional force on the Raman mode [79, 80]. In contrast, the quartic $d_{22}Q_{\text{IR}}^2Q_R^2$ term governs the curvature modulation, leading to the observed stiffening of the energy profile as illustrated in Fig. 4(c).

These qualitative insights are quantitatively supported by the coupling coefficients listed in Table III. Among all examined IR modes, $B_3(7)$ exhibits the largest d_{22} and a strong c_{21} , consistent with its dominant influence on both curvature stiffening and minimum potential energy position shift. The consistency between the energy landscape in Fig. 4(c) and the extracted coefficients provides a coherent picture of anharmonic coupling and highlights $B_3(7)$ as the most effective IR-active mode for driving nonlinear modulation of the CDW amplitude mode.

VI. CONCLUSION

In this work, we have presented a detailed first-principles study of coherent phonon-driven control of the CDW state in the quasi-one-dimensional material $(\text{TaSe}_4)_2\text{I}$. By systematically exploring the zone-center phonon modes of its low-temperature CDW phase, we identified nine symmetry-preserving Raman-active modes capable of inducing a transition from a gapped CDW insulator to a topologically nontrivial Weyl semimetal state. Among these, the 2.51 THz amplitude mode $A(18)$ emerges as the most efficient driver of this transition, requiring minimal atomic displacement to suppress the Γ –Z gap to the meV scale. This mode primarily modu-

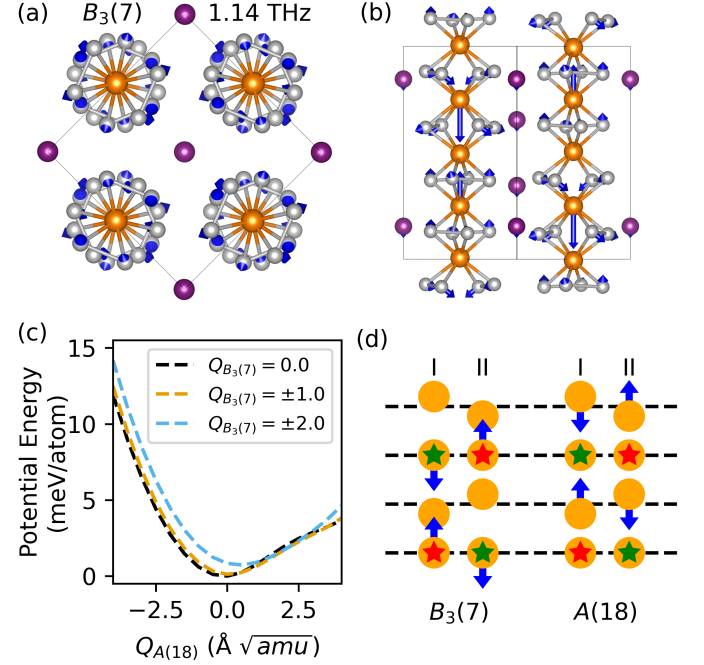


FIG. 4. Nonlinear coupling between the IR-active mode $B_3(7)$ and the CDW amplitude mode $A(18)$. (a) and (b) show the top and side views of the atomic displacements (eigenvectors) for the $B_3(7)$ mode, respectively, highlighting Ta atom vibrations along the c-axis, similar to the $A(18)$ mode. (c) Anharmonic potential energy surface of the Raman $A(18)$ mode modulated by the $B_3(7)$ IR mode. The three curves correspond to three different amplitudes of the $B_3(7)$ mode: the black dashed line represents $Q_{B_3(7)} = 0.0$, showing the baseline potential energy curve of $A(18)$ in the absence of IR distortion; the orange dashed line corresponds to $Q_{B_3(7)} = \pm 1.0$, where the energy landscape slightly stiffens; and the blue dashed line corresponds to $Q_{B_3(7)} = \pm 2.0$, showing a noticeable increase in curvature, indicating enhanced anharmonicity and stiffer restoring forces for $A(18)$. (d) Schematic comparison between the $B_3(7)$ and $A(18)$ modes, demonstrating the additional two-fold symmetry breaking caused by $B_3(7)$ mode displacement.

lates the Ta-tetramer chain structure, driving it toward a geometry closely resembling that of the non-CDW phase and enabling the reappearance of Weyl points.

While several higher-frequency Raman modes dominated by Se vibrations can likewise suppress the Γ –Z gap to the meV scale, they typically do so without substantially reducing the Ta-chain tetramerization, so that the underlying CDW lattice distortion largely remains intact. Moreover, these modes generally require significantly larger atomic displacements and are therefore less accessible under experimental conditions. This highlights the special role of $A(18)$ as an experimentally feasible and symmetry-compatible driver of topological switching.

From a topological perspective, the phonon-driven suppression of the Γ –Z gap is not merely a local feature of a high-symmetry line. We therefore use the minimum direct Γ –Z gap as a convenient indicator of gap quenching, and corroborate it with Brillouin-zone-wide Weyl-node

searches to establish the emergence of a globally gapless Weyl-semimetallic regime. For the 2.51 THz Raman mode $A(18)$, the BZ-wide search reveals Weyl nodes at generic k points; at the gap-minimizing distortion we identify 24 pairs of Weyl nodes. By contrast, the Se-dominated Raman A modes can also induce a Weyl-semimetallic regime, but typically with fewer Weyl-node pairs than $A(18)$, underscoring the exceptional efficiency of the CDW amplitude mode for lattice-driven topological restoration even when the Γ –Z gap remains finite at the meV scale.

Beyond identifying direct Raman pathways for the CDW-insulator-to-Weyl-semimetal transition, we investigated nonlinear phonon–phonon interactions and uncovered strong anharmonic coupling between $A(18)$ and the low-frequency IR-active mode $B_3(7)$ at 1.14 THz. This IR–Raman interaction includes a third-order term $c_{21}Q_{\text{IR}}^2Q_{\text{R}}$, which generates a displacive shift of the Raman-mode equilibrium coordinate, and a fourth-order term $d_{22}Q_{\text{IR}}^2Q_{\text{R}}^2$, which modulates the curvature of the $A(18)$ potential energy surface. Together, these effects enable IR-driven activation of symmetry-preserving Raman distortions and open an indirect, nonthermal pathway to control the CDW gap. This mechanism is particularly valuable for selective phonon control in time-resolved pump–probe experiments using THz pulses. Our predictions can be experimentally tested using state-of-the-art ultrafast nonlinear spectroscopies, especially recently developed THz pump–probe [82, 83] and THz two-dimensional coherent spectroscopy techniques [84–86]. These approaches have proven highly effective for probing collective modes [87–89] and coherent excitations [90] across a wide range of quantum materials.

Our study demonstrates a phonon-mode-selective route for nonthermal modulation of electronic topology in a CDW system. It provides quantitative metrics—including

phonon frequencies, displacement amplitudes, and anharmonic coupling coefficients—for guiding experimental access to ultrafast phase transitions. Furthermore, the IR–Raman hybrid driving scheme we propose expands the toolbox for dynamic materials control, especially in systems where direct Raman pumping is limited or energetically costly.

Together, these findings bridge lattice dynamics, topological band theory, and ultrafast condensed matter physics. They offer predictive guidance for coherent phase engineering in quantum materials, emphasizing the utility of low-frequency phonons and nonlinear coupling mechanisms. While our analysis focuses on $(\text{TaSe}_4)_2\text{I}$, the methodology and physical insights are broadly applicable to low-symmetry or low-dimensional quantum materials with strong electron–phonon coupling. Promising directions for future work include real-time phonon–electron simulations, ultrafast spectroscopy to validate IR–Raman activation pathways, and extension of this approach to symmetry-breaking phases such as magnetism, ferroelectricity, and superconductivity. These developments open new opportunities for designing THz-driven topological quantum devices.

ACKNOWLEDGEMENTS

This work was supported by the U.S. Department of Energy (DOE), Office of Science, Basic Energy Sciences, Materials Science and Engineering Division, including the grant of computer time at the National Energy Research Scientific Computing Center (NERSC) in Berkeley, California. The research was performed at the Ames National Laboratory, which is operated for the U.S. DOE by Iowa State University under Contract No. DE-AC02-07CH11358.

- [1] JI A Wilson, FJ Di Salvo, and S Mahajan, “Charge-density waves and superlattices in the metallic layered transition metal dichalcogenides,” *Adv. Phys.* **24**, 117–201 (1975).
- [2] George Gruner, *Density waves in solids* (CRC press, 2018).
- [3] K Rossnagel, “On the origin of charge-density waves in select layered transition-metal dichalcogenides,” *J. Phys.: Condens. Matter.* **23**, 213001 (2011).
- [4] Pierre Monceau, “Electronic crystals: an experimental overview,” *Adv. Phys.* **61**, 325–581 (2012).
- [5] Zo Z Wang, MC Saint-Lager, P Monceau, M Renard, P Gressier, A Meerschaut, L Guemas, and J Rouxel, “Charge density wave transport in (tase4) 2i,” *Solid State Commun.* **46**, 325–328 (1983).
- [6] H Fujishita, M Sato, and S Hoshino, “X-ray diffraction study of the quasi-one-dimensional conductors (mse4) 2i ($m = \text{ta}$ and nb),” *J. Phys. C: Solid State Phys.* **18**, 1105 (1985).
- [7] L Forró, JR Cooper, A Janossy, and M Maki, “Hall effect in the charge density wave system (tase4) 2i,” *Solid State Commun.* **62**, 715–718 (1987).
- [8] JE Lorenzo, R Currat, P Monceau, B Hennion, H Berger, and F Levy, “A neutron scattering study of the quasi-one-dimensional conductor,” *J. Phys.: Condens. Matter.* **10**, 5039 (1998).
- [9] L Németha, P Matus, G Kriza, and B Alavi, “Nmr in the pseudogap-and charge-density-wave states of (tase4) 2i,” *Synth. Met.* **200**, 600 (2001).
- [10] C Tournier-Colletta, L Moreschini, G Autes, S Moser, A Crepaldi, H Berger, AL Walter, KS Kim, A Bostwick, Pierre Monceau, *et al.*, “Electronic instability in a zero-gap semiconductor: The charge-density wave in (tase 4) 2 i,” *Phys. Rev. Lett.* **110**, 236401 (2013).
- [11] Alexander A Balandin, Fariborz Kargar, Tina T Salguero, and Roger K Lake, “One-dimensional van der waals quantum materials,” *Mater. Today* (2022), 10.1016/j.mattod.2022.03.015.
- [12] Jianwen Ma, Xianghao Meng, Binhua Zhang, Yuxiang Wang, Yicheng Mou, Wenting Lin, Yannan Dai, Luqiu Chen, Haonan Wang, Haoqi Wu, *et al.*, “Memristive switching in the surface of a charge–density–wave topo-

logical semimetal," *Sci. Bull.* **69**, 2042–2049 (2024).

[13] Subhajit Ghosh, Fariborz Kargar, Nick R Sesing, Zahra Barani, Tina T Salguero, Dong Yan, Sergey Rumyantsev, and Alexander A Balandin, "Low-frequency current fluctuations in quasi-1d (tase4) 2i weyl semimetal nanoribbons," *Adv. Electron. Mater.* **9**, 2200860 (2023).

[14] Jiaxin Cheng, Chao An, Liang Li, Lijie Chen, Yana Cui, Qijie Yan, Yanling Yin, Weichang Zhou, Yuehua Peng, Weike Wang, *et al.*, "High-performance near-infrared photodetector based on quasi one-dimensional layered (tase4) 2i," *Appl. Phys. Lett.* **119**, 201909 (2021).

[15] Zhenyang Xiao, Junqin Guo, Guangjian Liu, Jiaren Yuan, Xiaxia Liao, and Yangbo Zhou, "Light-driven conductivity in quasi-one-dimensional charge density wave insulator (tase4) 2i," *iscience* (2025), 10.1016/j.isci.2025.112647.

[16] Soyeun Kim, Yinchuan Lv, Xiao-Qi Sun, Chengxi Zhao, Nina Bielinski, Azel Murzabekova, Kejian Qu, Ryan A Duncan, Quynh LD Nguyen, Mariano Trigo, *et al.*, "Observation of a massive phason in a charge-density-wave insulator," *Nat. Mater.* **22**, 429–433 (2023).

[17] Di Cheng, Boqun Song, Jong-Hoon Kang, Chris Sundahl, Anthony L Edgeton, Liang Luo, Joong-Mok Park, Yesusa G Collantes, Eric E Hellstrom, Martin Mootz, *et al.*, "Study of elastic and structural properties of bafe2as2 ultrathin film using picosecond ultrasonics," *Materials* **16**, 7031 (2023).

[18] BQ Song, X Yang, C Sundahl, J-H Kang, M Mootz, Y Yao, IE Perakis, L Luo, CB Eom, and J Wang, "Ultrafast martensitic phase transition driven by intense terahertz pulses," *Ultrafast Science* **3**, 0007 (2023).

[19] Robert C McKay and Barry Bradlyn, "Optical response from charge-density waves in weyl semimetals," *Phys. Rev. B* **104**, 155120 (2021).

[20] Ryan A Duncan, Gal Orenstein, Soyeun Kim, Yijing Huang, Huaiyu Wang, Samuel W Teitelbaum, Jade Stanton, Matthew Hurley, Alexander Miller, Nicholas Leonard, *et al.*, "Coupled order parameters and photoinduced domain walls in the charge density wave of (tase4) 2i," *npj Quantum Mater.* **10**, 45 (2025).

[21] J Gooth, B Bradlyn, S Honnali, C Schindler, N Kumar, J Noky, Y Qi, C Shekhar, Y Sun, Z Wang, *et al.*, "Axionic charge-density wave in the weyl semimetal (tase4) 2i," *Nature* **575**, 315–319 (2019).

[22] Dan Sehayek, Manisha Thakurathi, and AA Burkov, "Charge density waves in weyl semimetals," *Phys. Rev. B* **102**, 115159 (2020).

[23] Wujun Shi, Benjamin J Wieder, Holger L Meyerheim, Yan Sun, Yang Zhang, Yiwei Li, Lei Shen, Yanpeng Qi, Lexian Yang, Jagannath Jena, *et al.*, "A charge-density-wave topological semimetal," *Nat. Phys.* **17**, 381–387 (2021).

[24] Wei-Chi Chiu, Guoqing Chang, Genneieve Macam, Ilya Belopolski, Shin-Ming Huang, Robert Markiewicz, Jia-Xin Yin, Zi-Jia Cheng, Chi-Cheng Lee, Tay-Rong Chang, *et al.*, "Causal structure of interacting weyl fermions in condensed matter systems," *Nat. Commun.* **14**, 2228 (2023).

[25] Jonathan B Curtis, Ioannis Petrides, and Prineha Narang, "Finite-momentum instability of a dynamical axion insulator," *Phys. Rev. B* **107**, 205118 (2023).

[26] Maksim Litskevich, Md Shafayat Hossain, Song-Bo Zhang, Zi-Jia Cheng, Satya N Guin, Nitesh Kumar, Chandra Shekhar, Zhiwei Wang, Yongkai Li, Guoqing Chang, *et al.*,

"Boundary modes of a charge density wave state in a topological material," *Nat. Phys.* **20**, 1253–1261 (2024).

[27] Utkarsh Khandelwal, Harshvardhan Jog, Shupeng Xu, Yicong Chen, Kejian Qu, Chengxi Zhao, Eugene J Mele, Daniel P Shoemaker, and Ritesh Agarwal, "Topological phase transition from optical manipulation of chiral response in the one-dimensional correlated weyl semimetal (tase 4) 2i," *Phys. Rev. B* **111**, 205108 (2025).

[28] Soyeun Kim, Robert C McKay, Nina Bielinski, Junehu Park, Chengxi Zhao, Meng-Kai Lin, Joseph A Hlevyack, Xuefei Guo, Sung-Kwan Mo, Peter Abbamonte, *et al.*, "Signatures of kramers-weyl fermions in the charge density wave material (tase4) 2i," *Communications Materials* **6**, 227 (2025).

[29] Chao An, Yonghui Zhou, Chunhua Chen, Fucong Fei, Fengqi Song, Changyong Park, Jianhui Zhou, Horst-Günter Rubahn, Victor V Moshchalkov, Xuliang Chen, *et al.*, "Long-range ordered amorphous atomic chains as building blocks of a superconducting quasi-one-dimensional crystal," *Adv. Mater.* **32**, 2002352 (2020).

[30] Qing-Ge Mu, Dennis Nenno, Yan-Peng Qi, Feng-Ren Fan, Cuiying Pei, Moaz ElGhazali, Johannes Gooth, Claudia Felser, Prineha Narang, and Sergey Medvedev, "Suppression of axionic charge density wave and onset of superconductivity in the chiral weyl semimetal ta 2 se 8 i," *Phys. Rev. Mater.* **5**, 084201 (2021).

[31] Jacob A Christensen, Simon Bettler, Kejian Qu, Jeffrey Huang, Soyeun Kim, Yinchuan Lu, Chengxi Zhao, Jin Chen, Matthew J Krogstad, Toby J Woods, *et al.*, "Disorder and diffuse scattering in single-chirality (tase 4) 2 i crystals," *Phys. Rev. Mater.* **8**, 034202 (2024).

[32] Zengle Huang, Hemian Yi, Lujin Min, Zhiqiang Mao, Cui-Zu Chang, and Weida Wu, "Absence of in-gap modes in charge density wave edge dislocations of the weyl semimetal (tase 4) 2 i," *Phys. Rev. B* **104**, 205138 (2021).

[33] Meng-Kai Lin, Joseph Andrew Hlevyack, Chengxi Zhao, Pavel Dudin, José Avila, Sung-Kwan Mo, Cheng-Maw Cheng, Peter Abbamonte, Daniel P Shoemaker, and Tai-Chang Chiang, "Unconventional spectral gaps induced by charge density waves in the weyl semimetal (tase4) 2i," *Nano Lett.* **24**, 8778–8783 (2024).

[34] F Yang and LQ Chen, "Microscopic phase-transition theory of charge density waves: revealing hidden transitions of phason and amplitudon," *arXiv preprint arXiv:2505.05025* (2025), 10.48550/arXiv.2505.05025.

[35] DN Basov, RD Averitt, and D Hsieh, "Towards properties on demand in quantum materials," *Nature materials* **16**, 1077–1088 (2017).

[36] Alberto de la Torre, Dante M Kennes, Martin Claassen, Simon Gerber, James W McIver, and Michael A Sentef, "Colloquium: Nonthermal pathways to ultrafast control in quantum materials," *Rev. Mod. Phys.* **93**, 041002 (2021).

[37] Liang Luo, Di Cheng, Boqun Song, Lin-Lin Wang, Chirag Vaswani, PM Lozano, G Gu, Chuankun Huang, Richard HJ Kim, Zhaoyu Liu, *et al.*, "A light-induced phononic symmetry switch and giant dissipationless topological photocurrent in ZrTe₅," *Nat. Mater.* **20**, 329–334 (2021).

[38] Liang Luo, Boqun Song, Genda Gu, Martin Mootz, Yongxin Yao, Ilias E Perakis, Qiang Li, and Jigang Wang, "Symmetry instability induced by topological phase transitions," *Physical Review B* **111**, 075151 (2025).

[39] Chirag Vaswani, L-L Wang, Dinusha Herath Mudiyanselage, Q Li, PM Lozano, GD Gu, Di Cheng, Boqun Song,

Liang Luo, Richard HJ Kim, *et al.*, “Light-driven raman coherence as a nonthermal route to ultrafast topology switching in a dirac semimetal,” *Phys. Rev. X* **10**, 021013 (2020).

[40] Tao Jiang, Peter P Orth, Liang Luo, Lin-Lin Wang, Feng Zhang, Cai-Zhuang Wang, Jin Zhao, Kai-Ming Ho, Jigang Wang, and Yong-Xin Yao, “Ab-initio simulations of coherent phonon-induced pumping of carriers in zirconium pentatelluride,” *Commun. Phys.* **6**, 297 (2023).

[41] Liang Luo, Xu Yang, X Liu, Zhiyan Liu, Chirag Vaswani, Di Cheng, M Mootz, Xin Zhao, Yongxin Yao, C-Z Wang, *et al.*, “Ultrafast manipulation of topologically enhanced surface transport driven by mid-infrared and terahertz pulses in bi2se3,” *Nat. Commun.* **10**, 607 (2019).

[42] Xu Yang, Liang Luo, Chirag Vaswani, Xin Zhao, Yongxin Yao, Di Cheng, Zhaoyu Liu, Richard HJ Kim, Xinyu Liu, Malgorzata Dobrowolska-Furdyna, *et al.*, “Light control of surface–bulk coupling by terahertz vibrational coherence in a topological insulator,” *npj Quantum Mater.* **5**, 13 (2020).

[43] Liang Luo, Di Cheng, Chuankun Huang, Xu Yang, Chirag Vaswani, Martin Mootz, Yongxin Yao, Xinyu Liu, Margaret Dobrowolska, Jacek K Furdyna, *et al.*, “Room temperature persisting surface charge carriers driven by intense terahertz electric fields in a topological insulator bi2se3,” *APL Materials* **11** (2023), 10.1063/5.0181223.

[44] Fei Sun, Qiong Wu, YL Wu, Hui Zhao, CJ Yi, YC Tian, HW Liu, YG Shi, Hong Ding, Xi Dai, *et al.*, “Coherent helix vacancy phonon and its ultrafast dynamics waning in topological dirac semimetal c d 3 a s 2,” *Physical Review B* **95**, 235108 (2017).

[45] Rishi Bhandia, David Barbalas, Run Xiao, Juan R Chamorro, Tanya Berry, Tyrel M McQueen, Nitin Samarth, and NP Armitage, “Anomalous electronic energy relaxation and soft phonons in the dirac semimetal cd 3 as 2,” *Physical Review B* **110**, 075131 (2024).

[46] Di Cheng, Tao Jiang, Feng Zhang, Genda Gu, Liang Luo, Chuankun Huang, Boqun Song, Martin Mootz, Avinash Khatri, Joong-Mok Park, *et al.*, “Revealing fano resonance in the dirac material zrte 5 through raman scattering,” *Phys. Rev. B* **112**, 075108 (2025).

[47] Daniel Werdehausen, Tomohiro Takayama, Marc Höppner, Gelon Albrecht, Andreas W Rost, Yangfan Lu, Dirk Manske, Hidenori Takagi, and Stefan Kaiser, “Coherent order parameter oscillations in the ground state of the excitonic insulator ta2nise5,” *Sci. Adv.* **4**, eaap8652 (2018).

[48] Julian Maklar, Jit Sarkar, Shuo Dong, Yaroslav A Gerasimenko, Tommaso Pincelli, Samuel Beaulieu, Patrick S Kirchmann, Jonathan A Sobota, Shuolong Yang, Dominik Leuenberger, *et al.*, “Coherent light control of a metastable hidden state,” *Sci. Adv.* **9**, eadi4661 (2023).

[49] Jiazila Hasain, Yanling Wu, Mengzhu Shi, Yanni Zhai, Qiong Wu, Zheng Liu, Yi Zhou, Xianhui Chen, and Jimin Zhao, “Emergent quantum state unveiled by ultrafast collective dynamics in 1 t-tas2,” *Proceedings of the National Academy of Sciences* **122**, e2406464122 (2025).

[50] Y Liu, YY Li, S Rajput, D Gilks, Leonardo Lari, PL Galindo, M Weinert, VK Lazarov, and L Li, “Tuning dirac states by strain in the topological insulator bi 2 se 3,” *Nat. Phys.* **10**, 294–299 (2014).

[51] Leslie M Schoop, Mazhar N Ali, Carola Straßer, Andreas Topp, Andrei Varykhalov, Dmitry Marchenko, Viola Duppel, Stuart SP Parkin, Bettina V Lotsch, and Christian R Ast, “Dirac cone protected by non-symmorphic symmetry and three-dimensional dirac line node in zrsis,” *Nat. Commun.* **7**, 11696 (2016).

[52] BQ Song, JDH Smith, T Jiang, YX Yao, and J Wang, “Quantum geometry embedded in unitarity of evolution: Revealing its impacts as geometric oscillation and dephasing in spin resonance and crystal bands,” *Phys. Rev. B* **111**, 144305 (2025).

[53] Bing Cheng, Di Cheng, Tao Jiang, Wei Xia, Boqun Song, Martin Mootz, Liang Luo, Ilias E Perakis, Yongxin Yao, Yanfeng Guo, *et al.*, “Chirality manipulation of ultrafast phase switches in a correlated cdw-weyl semimetal,” *Nat. Commun.* **15**, 785 (2024).

[54] Peter E Blöchl, “Projector augmented-wave method,” *Phys. Rev. B* **50**, 17953 (1994).

[55] John P Perdew, Kieron Burke, and Matthias Ernzerhof, “Generalized gradient approximation made simple,” *Phys. Rev. Lett.* **77**, 3865 (1996).

[56] Georg Kresse and Jürgen Furthmüller, “Efficient iterative schemes for ab initio total-energy calculations using a plane-wave basis set,” *Phys. Rev. B* **54**, 11169 (1996).

[57] H Fujishita, M Sato, and S Hoshino, “Incommensurate superlattice reflections in quasi one dimensional conductors,(mse4) 2 i (m= ta and nb),” *Solid State Commun.* **49**, 313–316 (1984).

[58] Atsushi Togo and Isao Tanaka, “First principles phonon calculations in materials science,” *Ser. Mater.* **108**, 1–5 (2015).

[59] Atsushi Togo, Kohei Shinohara, and Isao Tanaka, “Spglib: a software library for crystal symmetry search,” *Sci. technol. adv. material. Meth.* **4**, 2384822 (2024).

[60] Shyue Ping Ong, William Davidson Richards, Anubhav Jain, Geoffroy Hautier, Michael Kocher, Shreyas Cholia, Dan Gunter, Vincent L Chevrier, Kristin A Persson, and Gerbrand Ceder, “Python materials genomics (pymatgen): A robust, open-source python library for materials analysis,” *Comput. Mater. Sci.* **68**, 314–319 (2013).

[61] Mois I Aroyo, Asen Kirov, Cesar Capillas, JM Perez-Mato, and Hans Wondratschek, “Bilbao crystallographic server. ii. representations of crystallographic point groups and space groups,” *Acta Crystallogr. A* **62**, 115–128 (2006).

[62] Nicola Marzari and David Vanderbilt, “Maximally localized generalized wannier functions for composite energy bands,” *Phys. Rev. B* **56**, 12847 (1997).

[63] Ivo Souza, Nicola Marzari, and David Vanderbilt, “Maximally localized wannier functions for entangled energy bands,” *Phys. Rev. B* **65**, 035109 (2001).

[64] MP Lopez Sancho, JM Lopez Sancho, JM Lopez Sancho, and J Rubio, “Highly convergent schemes for the calculation of bulk and surface green functions,” *J. Phys. F: Metal Phys.* **15**, 851 (1985).

[65] QuanSheng Wu, ShengNan Zhang, Hai-Feng Song, Matthias Troyer, and Alexey A Soluyanov, “Wannier-tools: An open-source software package for novel topological materials,” *Comput. Phys. Commun.* **224**, 405–416 (2018).

[66] Yang Zhang, Ling-Fang Lin, Adriana Moreo, Shuai Dong, and Elbio Dagotto, “First-principles study of the low-temperature charge density wave phase in the quasi-one-dimensional weyl chiral compound (tase 4) 2 i,” *Phys. Rev. B* **101**, 174106 (2020).

[67] Hanjo Schäfer, Michael Körber, Andrej Tomeljak, K Biljaković, Helmut Berger, and Jure Demsar, “Dynamics of charge density wave order in the quasi one dimen-

sional conductor (tase4) 2i probed by femtosecond optical spectroscopy," *Eur. Phys. J. Spec. Top.* **222**, 1005–1016 (2013).

[68] Wibke Bronsch, Manuel Tuniz, Giuseppe Crupi, Michela De Col, Denny Puntel, Davide Soranzio, Alessandro Giammari, Michele Perlangeli, Helmuth Berger, Dario De Angelis, *et al.*, "Ultrafast dynamics in (tase 4) 2 i triggered by valence and core-level excitation," *Faraday Discuss.* **237**, 40–57 (2022).

[69] Xiao-Ping Li, Ke Deng, Botao Fu, YongKai Li, Da-Shuai Ma, JunFeng Han, Jianhui Zhou, Shuyun Zhou, and Yugui Yao, "Type-iii weyl semimetals:(tase 4) 2 i," *Phys. Rev. B* **103**, L081402 (2021).

[70] Richard HJ Kim, Chuankun Huang, Yilong Luan, Lin-Lin Wang, Zhaoyu Liu, Joong-Mok Park, Liang Luo, Pedro M Lozano, Genda Gu, Deniz Turan, *et al.*, "Terahertz nano-imaging of electronic strip heterogeneity in a dirac semimetal," *ACS photonics* **8**, 1873–1880 (2021).

[71] Michael Först, Cristian Manzoni, Stefan Kaiser, Yasuhide Tomioka, Yoshi-nori Tokura, Roberto Merlin, and Andrea Cavalleri, "Nonlinear phononics as an ultrafast route to lattice control," *Nat. Phys.* **7**, 854–856 (2011).

[72] Di Cheng, Zhiyan Liu, Liang Luo, Chirag Vaswani, J-M Park, Yongxin Yao, Z Song, Chuankun Huang, D-H Mudiyanselage, RHJ Kim, *et al.*, "Helicity-dependent terahertz photocurrent and phonon dynamics in hybrid metal halide perovskites," *The Journal of Chemical Physics* **151** (2019), 10.1063/1.5127767.

[73] Zhaoyu Liu, Chirag Vaswani, Liang Luo, Di Cheng, X Yang, Xin Zhao, Yongxin Yao, Z Song, Roberto Brenes, RJH Kim, *et al.*, "Coherent band-edge oscillations and dynamic longitudinal-optical phonon mode splitting as evidence for polarons in perovskites," *Physical Review B* **101**, 115125 (2020).

[74] Zhaoyu Liu, Chirag Vaswani, X Yang, X Zhao, Yongxin Yao, Z Song, Di Cheng, Y Shi, Liang Luo, D-H Mudiyanselage, *et al.*, "Ultrafast control of excitonic rashba fine structure by phonon coherence in the metal halide perovskite ch 3 nh 3 pbi 3," *Physical Review Letters* **124**, 157401 (2020).

[75] Zhaoyu Liu, Y Shi, T Jiang, Liang Luo, C Huang, Martin Mootz, Z Song, Y Yan, Yongxin Yao, J Zhao, *et al.*, "Coherent transfer of lattice entropy via extreme nonlinear phononics in metal halide perovskites," *PRX Energy* **3**, 023009 (2024).

[76] Guru Khalsa and Nicole A Benedek, "Ultrafast optically induced ferromagnetic/anti-ferromagnetic phase transition in gdtio3 from first principles," *npj Quantum Mater.* **3**, 15 (2018).

[77] Nan Feng, Jian Han, Changpeng Lin, Zhengwei Ai, Chuwen Lan, Ke Bi, Yuanhua Lin, Kan-Hao Xue, and Ben Xu, "Anti-jahn-teller effect induced ultrafast insulator to metal transition in perovskite babio3," *npj Comput. Mater.* **8**, 226 (2022).

[78] Rui Tang, Filippo Boi, and Yi-Han Cheng, "Light-induced topological phase transition via nonlinear phononics in superconductor csv3sb5," *npj Quantum Mater.* **8**, 78 (2023).

[79] Alaska Subedi, Andrea Cavalleri, and Antoine Georges, "Theory of nonlinear phononics for coherent light control of solids," *Phys. Rev. B* **89**, 220301 (2014).

[80] Alaska Subedi, "Proposal for ultrafast switching of ferroelectrics using midinfrared pulses," *Phys. Rev. B* **92**, 214303 (2015).

[81] Michael Fechner and Nicola A Spaldin, "Effects of intense optical phonon pumping on the structure and electronic properties of yttrium barium copper oxide," *Phys. Rev. B* **94**, 134307 (2016).

[82] X Yang, C Vaswani, C Sundahl, M Mootz, L Luo, JH Kang, IE Perakis, CB Eom, and J Wang, "Lightwave-driven gapless superconductivity and forbidden quantum beats by terahertz symmetry breaking," *Nature Photonics* **13**, 707–713 (2019).

[83] M Mootz, C Vaswani, C Huang, KJ Lee, A Khatri, P Mandal, JH Kang, L Luo, IE Perakis, CB Eom, *et al.*, "Observation of superconducting solitons by terahertz-light-driven persistent pseudo-spin coherence," *arXiv preprint arXiv:2507.22383* (2025), 10.48550/arXiv.2507.22383.

[84] Martin Mootz, Liang Luo, Jigang Wang, and Ilias E Perakis, "Visualization and quantum control of light-accelerated condensates by terahertz multi-dimensional coherent spectroscopy," *Communications Physics* **5**, 47 (2022).

[85] L Luo, M Mootz, Jong-Hoon Kang, Chuankun Huang, Kitae Eom, JW Lee, C Vaswani, YG Collantes, EE Hellstrom, Ilias E Perakis, *et al.*, "Quantum coherence tomography of light-controlled superconductivity," *Nature Physics* **19**, 201–209 (2023).

[86] Chuankun Huang, Martin Mootz, Liang Luo, Ilias E Perakis, and Jigang Wang, "Terahertz 2d coherent spectroscopy for probing and controlling multicorrelations in quantum matter," *Nature Reviews Physics* (2026), 10.1038/s42254-025-00917-2.

[87] Bing Cheng, Di Cheng, Kyuho Lee, Liang Luo, Zhuoyu Chen, Yonghun Lee, Bai Yang Wang, Martin Mootz, Ilias E Perakis, Zhi-Xun Shen, *et al.*, "Evidence for d-wave superconductivity of infinite-layer nickelates from low-energy electrodynamics," *Nature Materials* **23**, 775–781 (2024).

[88] Chuankun Huang, L Luo, Martin Mootz, J Shang, P Man, L Su, Ilias E Perakis, YX Yao, A Wu, and Jigang Wang, "Extreme terahertz magnon multiplication induced by resonant magnetic pulse pairs," *Nature Communications* **15**, 3214 (2024).

[89] Chuankun Huang, Martin Mootz, Liang Luo, Di Cheng, Avinash Khatri, Joong-Mok Park, Richard HJ Kim, Yihua Qiang, Victor L Quito, Yongxin Yao, *et al.*, "Discovery of an unconventional quantum echo by interference of higgs coherence," *Science Advances* **11**, eads8740 (2025).

[90] X Yang, C Vaswani, C Sundahl, M Mootz, P Gagel, L Luo, JH Kang, PP Orth, IE Perakis, CB Eom, *et al.*, "Terahertz-light quantum tuning of a metastable emergent phase hidden by superconductivity," *Nature materials* **17**, 586–591 (2018).

Appendix A: Direct-gap collapse on different high-symmetry paths

To justify using the minimum direct Γ –Z gap as the primary indicator in the main text, we compared the evolution of the minimum direct band gap along several representative high-symmetry paths, including Γ –Z, X – G_0 –H₀–Y, and Γ –L, as a function of the normal-mode amplitude Q for the same set of frozen-phonon distortions. For each distorted structure, we extracted the minimum

direct gap along each path by scanning the band energies on the same k -point sampling and using identical electronic-structure settings as in the main text. As shown in Fig. A1, the direct gaps along Γ –Z and X – G_0 – H_0 –Y are, in general, suppressed much more rapidly with increasing Q than the gap along Γ –L. For most Raman modes, the Γ –Z gap collapses at a rate comparable to or faster than the X – G_0 – H_0 –Y gap. Two minor exceptions are the CDW amplitude mode $A(18)$, mode $A(30)$ and mode $A(40)$, for which X – G_0 – H_0 –Y decreases marginally faster than Γ –Z over a limited range of small-to-intermediate Q . Any deviations from this trend are marginal and restricted to a limited Q window, and therefore do not affect the conclusions drawn below. In particular, for $A(18)$ the minimum gap along X – G_0 – H_0 –Y reaches the near-closure regime at $Q \simeq 2.2 \text{ \AA}\sqrt{\text{amu}}$, slightly earlier than along Γ –Z (near $Q \simeq 2.5 \text{ \AA}\sqrt{\text{amu}}$). This earlier suppression indicates that the system can enter a Weyl-semimetallic regime with nodes emerging first in the vicinity of G_0 – H_0 , although the number of Weyl points in this regime is limited. Importantly, this subtle path-dependent difference does not affect our main conclusions: the emergence of Weyl nodes is established by Brillouin-zone-wide searches, and Weyl points already appear at $Q = 2.0 \text{ \AA}\sqrt{\text{amu}}$ even before the Γ –Z direct gap reaches its near-closure minimum. A similar, weak preference of X – G_0 – H_0 –Y is observed for $A(30)$ and $A(40)$. In contrast, the Γ –L gap decreases more slowly and typically remains finite over the same distortion range, demonstrating a reduced sensitivity to the phonon-driven lattice modulation. Taken together, these comparisons support the use of the minimum direct Γ –Z gap as a robust and consistent indicator across all Raman modes. This trend is consistent with the quasi-one-dimensional nature of $(\text{TaSe}_4)_2\text{I}$, where the CDW distortion predominantly modulates electronic states dispersing along the chain direction (reciprocal c^*), making Γ –Z particularly responsive to the CDW-induced gap opening and its phonon-driven collapse. Therefore, the minimum direct Γ –Z gap provides a reliable proxy for tracking the approach to the topological transition discussed in the main text.

Appendix B: Element-resolved weights of the Γ –Z bands

To characterize the elemental composition of the near-gap electronic states, we projected the band weights onto Ta, Se, and I along the Γ –Z path for the equilibrium CDW structure ($Q = 0$) and for the $A(18)$ -distorted structure at $Q = 2.5 \text{ \AA}\sqrt{\text{amu}}$ (Fig. A2). The color intensity encodes the normalized projected weight of a given element for each Kohn–Sham band state along Γ –Z, where values closer to 1 indicate a stronger contribution from that element. For both $Q = 0$ and $Q = 2.5$, the states forming the valence-band maximum and conduction-band minimum are dominated by Ta weight with a secondary Se contribution, while the I contribution remains negligible near

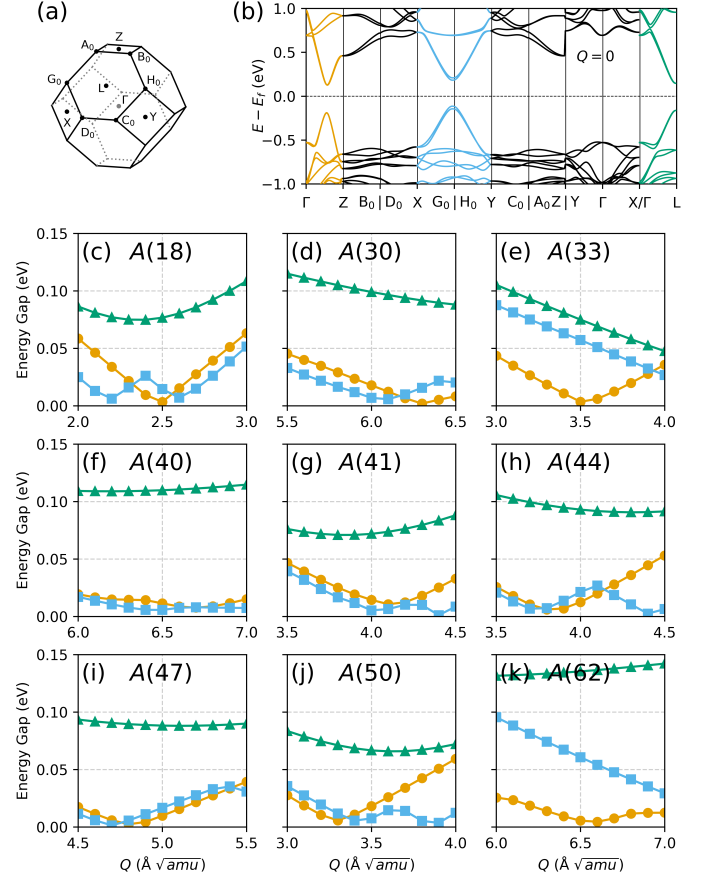


FIG. A1. Direct-gap response on different high-symmetry paths under frozen-phonon distortions in the F222 CDW phase of $(\text{TaSe}_4)_2\text{I}$. (a) Brillouin zone and the high-symmetry points used in this section. (b) Electronic band structure at equilibrium ($Q = 0$) along the selected high-symmetry paths; the colored segments highlight the three paths used for direct-gap tracking: Γ –Z (yellow), X – G_0 | H_0 –Y (blue), and Γ –L (green). (c)–(k) Minimum direct band gap as a function of the normal-mode amplitude Q for representative Raman-active A modes, comparing the three paths on the same energy scale and with identical electronic-structure settings as in the main text.

the Fermi level. This element-resolved analysis supports the conclusion that the $A(18)$ -induced gap suppression is primarily governed by distortions that strongly affect the Ta-derived near-gap bands, with Se providing a weaker but non-negligible modulation.

Appendix C: Element-resolved contribution of the $A(18)$ mode to gap suppression

To further clarify the microscopic origin of the $A(18)$ -driven gap suppression, we analyzed the element-resolved character of the $A(18)$ lattice distortion. We decomposed the $A(18)$ eigenvector into element-resolved components by constructing “Ta-only” and “Se-only” frozen-phonon distortions (Fig. A3). In the Ta-only distortion, only

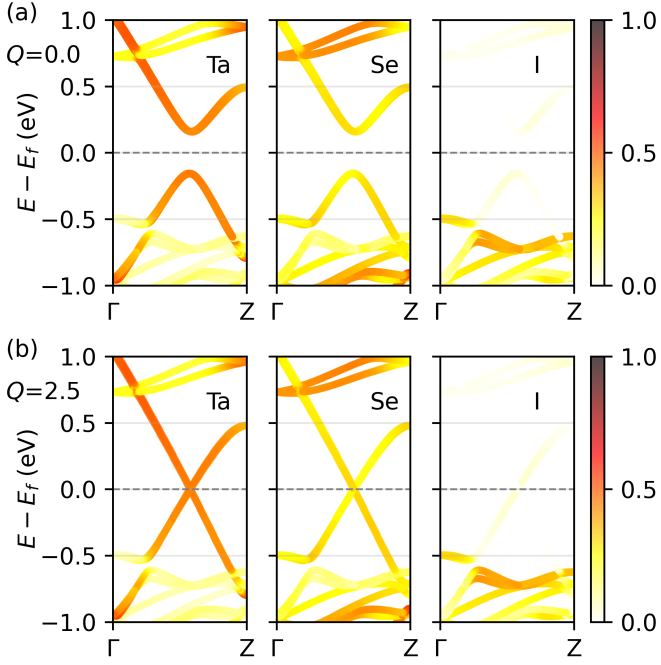


FIG. A2. Element-resolved projected band weights along Γ -Z for $(\text{TaSe}_4)_2\text{I}$. (a) Equilibrium CDW structure ($Q = 0$). (b) $A(18)$ -distorted structure at $Q = 2.5 \text{ \AA}\sqrt{\text{amu}}$. For each structure, the three panels show the Ta-, Se-, and I-projected weights, respectively. The color scale indicates the normalized projected weight (0–1) of the corresponding element for each Kohn–Sham band state along Γ -Z.

Ta atoms are displaced following the $A(18)$ eigenvector direction while Se and I atoms are fixed [Fig. A3(a)]; conversely, the Se-only distortion displaces only Se atoms while Ta and I atoms remain fixed [Fig. A3(b)]. In both cases we keep the same normalization of the normal-mode coordinate $Q_{A(18)}$ as in the full-mode distortion to enable a direct comparison.

Figures A3(c) and A3(d) show the evolution of the minimum direct gap along Γ -Z, $E_G(\Gamma\text{-Z})$, as a function of $Q_{A(18)}$ for the Ta-only and Se-only distortions, respectively. The Ta-only distortion produces a pronounced suppression of the Γ -Z gap and already reduces it to the meV scale at $Q_{A(18)} = 2.0 \text{ \AA}\sqrt{\text{amu}}$, which is smaller than the amplitude required for the full $A(18)$ mode ($Q_{A(18)} = 2.5 \text{ \AA}\sqrt{\text{amu}}$). By contrast, the Se-only distortion drives the gap in the opposite direction and yields a weak *increase* of $E_G(\Gamma\text{-Z})$ for $Q > 0$. This opposite trend demonstrates that the Se contribution enters with the opposite sign in the gap modulation and thus partially counteracts the Ta-driven gap suppression in the full mode, consistent with the Ta-only and Se-only frozen-phonon tests. Figure A3(e) shows the corresponding Γ -Z band structure for the Ta-only distortion at $Q_{A(18)} = 2.0 \text{ \AA}\sqrt{\text{amu}}$ (marked in Fig. A3(c)), where the minimum direct gap is reduced to the meV scale; the magnified inset resolves the residual gap near E_F .

A Brillouin-zone-wide Weyl-node search based on the

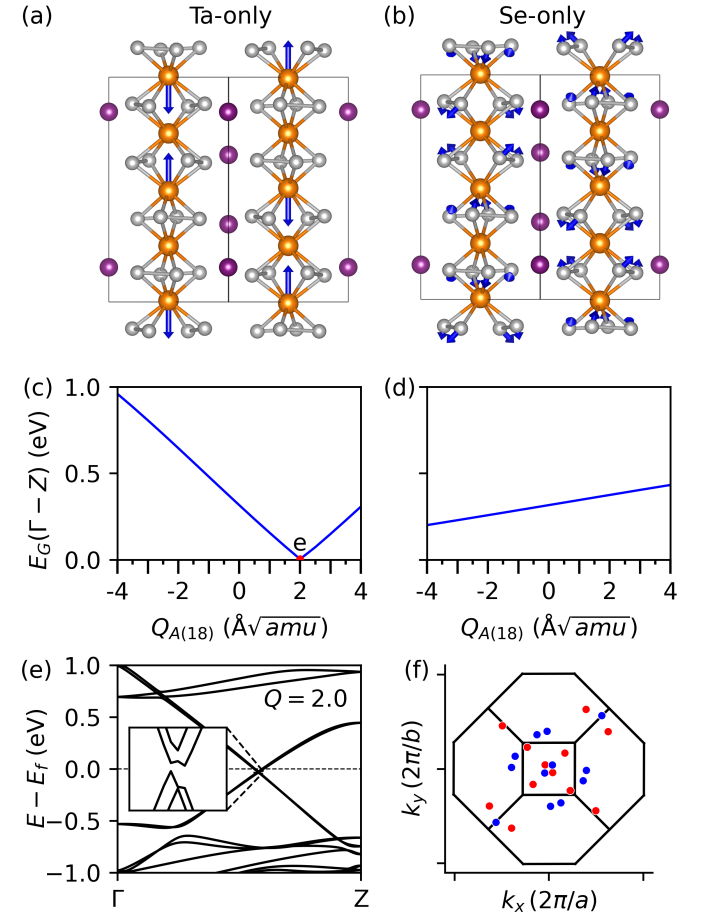


FIG. A3. Element-selective decomposition of the CDW amplitude mode $A(18)$ and its distinct impacts on the Γ -Z gap and Weyl topology. (a) Ta-only distortion constructed by keeping only the Ta atomic displacements from the full $A(18)$ eigenvector (Se and I atoms fixed). (b) Se-only distortion constructed by keeping only the Se displacements (Ta and I fixed). (c),(d) Evolution of the minimum direct gap along Γ -Z, $E_G(\Gamma\text{-Z})$, as a function of the normal-mode coordinate $Q_{A(18)}$ for the Ta-only and Se-only distortions in (a) and (b), respectively. (e) Electronic band structure along Γ -Z at the Ta-only distortion marked in (c), where the minimum direct Γ -Z gap is suppressed to 2.0 meV and the residual opening is resolved in the magnified inset. The inset shows a magnified view in the energy window $E - E_F \in [-0.05, -0.01] \text{ eV}$. (f) Corresponding Weyl-node distribution obtained from a Brillouin-zone-wide search for the Ta-only distorted structure in (e), shown as a k_x - k_y projection; red and blue spheres denote Weyl nodes with positive and negative chiral charge, respectively.

Wannier Hamiltonian identifies Weyl nodes at generic k points for this Ta-only distorted structure, and their k_x - k_y projection is shown in Fig. A3(f). Taken together, these results indicate that the $A(18)$ mode couples to the gap through opposite-signed element-resolved contributions: Ta motion provides the leading gap-suppression channel, whereas Se motion provides a weaker gap-opening modulation, so that the net critical amplitude reflects

a competition between Ta and Se displacements rather than Ta-Ta geometry alone.

Appendix D: Zone-Center Phonon Modes of $(\text{TaSe}_4)_2\text{I}$ in the CDW Phase

We list all zone-center phonon modes of $(\text{TaSe}_4)_2\text{I}$ in its CDW phase (space group $F2\bar{2}\bar{2}$), including their vibrational frequencies, irreducible representations, and optical activity. This table provides the mode indices used throughout the main text, including the Raman-active CDW amplitude mode $A(18)$ at 2.51 THz and the additional symmetry-preserving Raman A modes ($A(30)$, $A(33)$, $A(40)$, $A(41)$, $A(44)$, $A(47)$, $A(50)$, and $A(62)$) that are dominated by Se vibrations. We also report the space group retained after displacing atoms along each phonon eigenvector (SG_{disp}), which is used to distinguish

symmetry-preserving and symmetry-breaking distortions.

Appendix E: Anharmonic Coupling Between IR-Active Phonons and the CDW Amplitude Mode $A(18)$

This section summarizes the anharmonic coupling coefficients between *all* infrared-active phonon modes and the Raman-active CDW amplitude mode $A(18)$, extracted from the fourth-order nonlinear phonon potential in Eq. (2). The coefficients are obtained by fitting the two-dimensional energy surface $V(Q_{\text{IR}}, Q_{\text{R}})$ computed from frozen-phonon DFT calculations (energy in meV per atom). For clarity, we list only symmetry-allowed, nonzero terms; coefficients associated with odd powers of Q_{IR} vanish for all IR B modes. Among all IR modes, mode 7 shows the strongest cubic and quartic IR-Raman couplings and is referred to as $B_3(7)$ in the main text.

TABLE A1. Zone-center phonon modes of $(\text{TaSe}_4)_2\text{I}$ in the CDW phase ($F2\bar{2}2$), including vibrational frequencies (THz), irreducible representations (Irrep), optical activity, and the space group retained after displacing atoms along each phonon eigenvector (SG_{disp}).

Idx	Freq	Irrep	Activity	SG _{disp}	Idx	Freq	Irrep	Activity	SG _{disp}	Idx	Freq	Irrep	Activity	SG _{disp}
1	0.00	<i>B</i> ₂	Acoustic	<i>F</i> 222	23	3.10	<i>B</i> ₁	IR,Raman	<i>C</i> 2	45	5.10	<i>B</i> ₂	IR,Raman	<i>C</i> 2
2	0.00	<i>B</i> ₁	Acoustic	<i>F</i> 222	24	3.21	<i>B</i> ₂	IR,Raman	<i>C</i> 2	46	5.25	<i>B</i> ₃	IR,Raman	<i>C</i> 2
3	0.00	<i>B</i> ₃	Acoustic	<i>F</i> 222	25	3.25	<i>B</i> ₁	IR,Raman	<i>C</i> 2	47	5.34	<i>A</i>	Raman	<i>F</i> 222
4	1.01	<i>B</i> ₁	IR,Raman	<i>C</i> 2	26	3.71	<i>B</i> ₃	IR,Raman	<i>C</i> 2	48	5.47	<i>B</i> ₂	IR,Raman	<i>C</i> 2
5	1.04	<i>B</i> ₃	IR,Raman	<i>C</i> 2	27	3.95	<i>B</i> ₂	IR,Raman	<i>C</i> 2	49	5.49	<i>B</i> ₁	IR,Raman	<i>C</i> 2
6	1.06	<i>B</i> ₂	IR,Raman	<i>C</i> 2	28	3.97	<i>B</i> ₁	IR,Raman	<i>C</i> 2	50	5.50	<i>A</i>	Raman	<i>F</i> 222
7	1.14	<i>B</i> ₃	IR,Raman	<i>C</i> 2	29	4.01	<i>B</i> ₃	IR,Raman	<i>C</i> 2	51	5.65	<i>B</i> ₂	IR,Raman	<i>C</i> 2
8	1.27	<i>B</i> ₂	IR,Raman	<i>C</i> 2	30	4.07	<i>A</i>	Raman	<i>F</i> 222	52	5.67	<i>B</i> ₃	IR,Raman	<i>C</i> 2
9	1.29	<i>B</i> ₁	IR,Raman	<i>C</i> 2	31	4.16	<i>B</i> ₁	IR,Raman	<i>C</i> 2	53	5.86	<i>B</i> ₃	IR,Raman	<i>C</i> 2
10	1.54	<i>B</i> ₂	IR,Raman	<i>C</i> 2	32	4.23	<i>B</i> ₂	IR,Raman	<i>C</i> 2	54	5.87	<i>B</i> ₁	IR,Raman	<i>C</i> 2
11	1.58	<i>B</i> ₁	IR,Raman	<i>C</i> 2	33	4.23	<i>A</i>	Raman	<i>F</i> 222	55	6.11	<i>B</i> ₂	IR,Raman	<i>C</i> 2
12	1.60	<i>B</i> ₁	IR,Raman	<i>C</i> 2	34	4.30	<i>B</i> ₃	IR,Raman	<i>C</i> 2	56	6.28	<i>B</i> ₁	IR,Raman	<i>C</i> 2
13	1.62	<i>B</i> ₂	IR,Raman	<i>C</i> 2	35	4.44	<i>A</i>	Raman	<i>F</i> 222	57	6.66	<i>B</i> ₁	IR,Raman	<i>C</i> 2
14	1.67	<i>B</i> ₃	IR,Raman	<i>C</i> 2	36	4.48	<i>B</i> ₂	IR,Raman	<i>C</i> 2	58	6.75	<i>B</i> ₂	IR,Raman	<i>C</i> 2
15	1.82	<i>A</i>	Raman	<i>F</i> 222	37	4.50	<i>B</i> ₁	IR,Raman	<i>C</i> 2	59	7.76	<i>B</i> ₂	IR,Raman	<i>C</i> 2
16	1.91	<i>A</i>	Raman	<i>F</i> 222	38	4.50	<i>B</i> ₃	IR,Raman	<i>C</i> 2	60	7.81	<i>B</i> ₁	IR,Raman	<i>C</i> 2
17	2.01	<i>B</i> ₃	IR,Raman	<i>C</i> 2	39	4.74	<i>B</i> ₃	IR,Raman	<i>C</i> 2	61	7.84	<i>B</i> ₃	IR,Raman	<i>C</i> 2
18	2.51	<i>A</i>	Raman	<i>F</i> 222	40	4.82	<i>A</i>	Raman	<i>F</i> 222	62	7.84	<i>A</i>	Raman	<i>F</i> 222
19	2.71	<i>B</i> ₁	IR,Raman	<i>C</i> 2	41	4.84	<i>A</i>	Raman	<i>F</i> 222	63	7.91	<i>A</i>	Raman	<i>F</i> 222
20	2.73	<i>A</i>	Raman	<i>F</i> 222	42	4.90	<i>B</i> ₃	IR,Raman	<i>C</i> 2	64	8.05	<i>B</i> ₃	IR,Raman	<i>C</i> 2
21	2.79	<i>B</i> ₂	IR,Raman	<i>C</i> 2	43	4.97	<i>B</i> ₁	IR,Raman	<i>C</i> 2	65	8.13	<i>B</i> ₂	IR,Raman	<i>C</i> 2
22	3.07	<i>B</i> ₂	IR,Raman	<i>C</i> 2	44	5.08	<i>A</i>	Raman	<i>F</i> 222	66	8.17	<i>B</i> ₁	IR,Raman	<i>C</i> 2

TABLE A2. Complete list of anharmonic coupling coefficients between *all* IR-active phonon modes and the Raman-active CDW amplitude mode $A(18)$ in $(\text{TaSe}_4)_2\text{I}$. Listed are the mode indices and selected coefficients ($c_2, c_{21}, d_1, d_2, d_{22}$) from the nonlinear energy expansion. Coefficients not included in this table are c_1, c_{12}, d_{13} , and d_{31} , as they are zero for all modes.